Accepted Manuscript

Design and characterization of nano and bimodal structured biodegradable Fe-Mn-Ag alloy with accelerated corrosion rate

Pedram Sotoudeh Bagha, Mehrdad Khakbiz, Saeed Sheibani, Hendra Hermawan

PII: S0925-8388(18)32707-5

DOI: 10.1016/j.jallcom.2018.07.206

Reference: JALCOM 46922

To appear in: *Journal of Alloys and Compounds*

Received Date: 25 April 2018

Revised Date: 4 July 2018

Accepted Date: 17 July 2018

Please cite this article as: P. Sotoudeh Bagha, M. Khakbiz, S. Sheibani, H. Hermawan, Design and characterization of nano and bimodal structured biodegradable Fe-Mn-Ag alloy with accelerated corrosion rate, *Journal of Alloys and Compounds* (2018), doi: 10.1016/j.jallcom.2018.07.206.

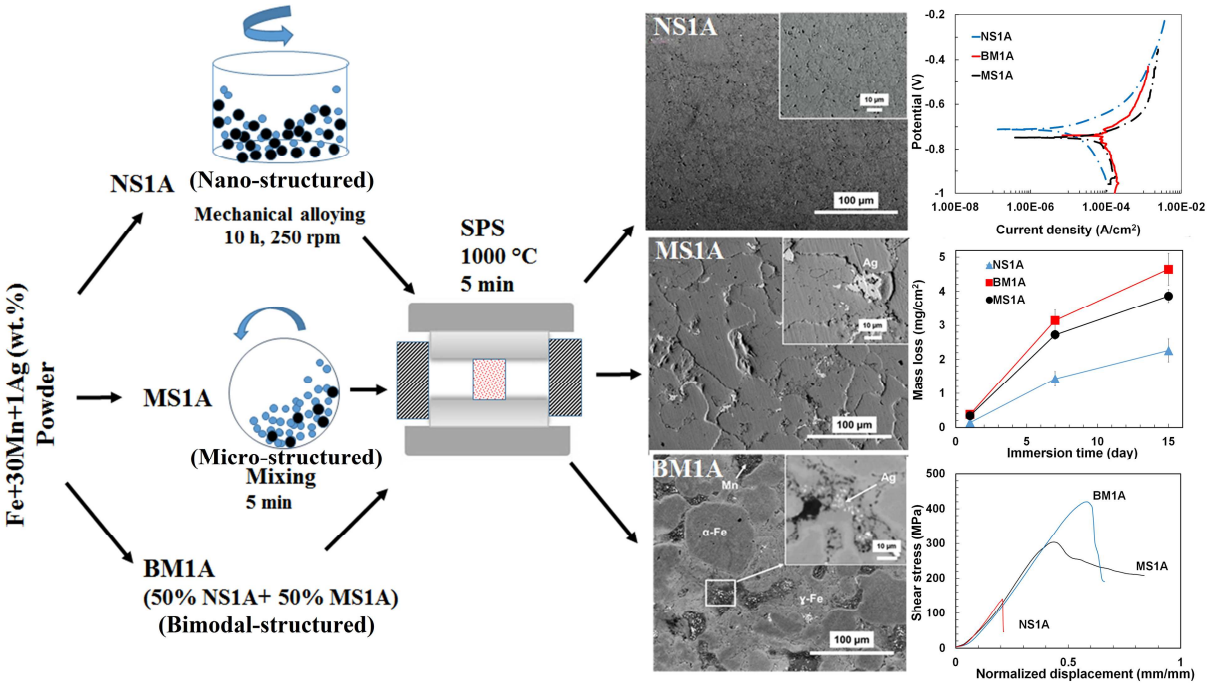

Design and characterization of nano and bimodal structured biodegradable Fe-Mn-Ag alloy with accelerated corrosion rate

Pedram Sotoudeh Bagha [1], Mehrdad Khakbiz [1, *], Saeed Sheibani [2], Hendra Hermawan [3, *]

[1] Division of Biomedical Engineering, Department of Life Science Engineering, Faculty of New Sciences and Technologies, University of Tehran, Tehran, Iran.

[2] School of Metallurgy and Materials Engineering, College of Engineering, University of Tehran, Tehran, Iran.

[3] Department of Mining, Metallurgical and Materials Engineering & CHU de Quebec Research Center, Laval University, Quebec City, Canada.

*Corresponding authors:khakbiz@ut.ac.ir (Mehrdad Khakbiz),

hendra.hermawan@gmn.ulaval.ca (Hendra Hermawan)

Abstract

Researchers in biodegradable metals have been putting efforts to accelerate the corrosion of iron-based biodegradable metals. These include by alloying iron with manganese and noble elements such as silver, but further increase to the corrosion rate is still needed. In this study, a set of bimodal nano/microstructured Fe-30Mn-1Ag alloys was prepared through mechanical alloying and spark plasma sintering. The alloys were characterized and tested for their corrosion behavior in Hanks' solution at 37^{o}C and for their mechanical properties. The bimodal-structured alloy possessed a mixture of austenitic (γ-FeMn) and ferritic (α-Fe) phases, while the nano- and macro-structured ones were essentially composed of γ-FeMn and α-Fe phases, respectively. Addition of 1-3 wt.% of silver into the nanostructured alloy increased its corrosion rate from 0.24 mm/year to 0.33 and 0.58 mm/year for Fe-30Mn-1Ag and Fe-30Mn-3Ag, respectively. Whilst, the bimodal Fe-30Mn-1Ag alloy corroded at a higher rate of 0.88 mm/year. This alloy also possessed an interesting combination of high and low micro-hardness phases that contributed to high shear strength of 417 MPa and shear strain of 0.66. Detailed discussion on the relationship of microstructure with corrosion behavior and mechanical properties is presented in this manuscript.

Keywords: Biodegradable metals, bimodal structure, corrosion, Fe-Mn-Ag, spark plasma sintering

1. Introduction

Absorbable or biodegradable metals, metals that corrode in the in vivo environment, have been viewed as ideal candidate materials for load bearing temporary medical implants. They provide the necessary mechanical support during a healing process of treated tissue while degrade progressively leaving no residual implant thus avoid a second surgery [1]. Iron, magnesium, zinc and their alloys are considered in this new class of metallic biomaterials. Owing to its high strength, iron-based biodegradable metals have been considered for stent applications, however, its low corrosion rate still constitutes a major challenge [2]. Two in vivo studies on iron implants found that the formation of protective iron oxide/hydroxide/phosphate layers acted as a barrier against oxygen transport thus slow down the overall corrosion process [3,4].

Attempts to accelerate the corrosion of iron-based metals have been done by introducing new phases or noble particles into the iron matrix to create potential differences at the microscopic level. This was done by alloying iron with manganese, palladium, silver, gallium, gold and platinum [5–8] by various techniques such as vacuum plasma nitriding process [9], vapour vacuum arc technique [10] and magnetron sputtering [11]. A rather different approach, mostly suitable for porous iron, was done by making composite or iron with polymers where the hydrolysis of polymers created a local acidic environment that dissolve iron oxides [12–14]. Palladium and silver are two noble elements where their addition into iron-based metals is expected to form microgalvanic sites and thus increase the corrosion rate of the alloys. Huang et al [10] found that implantation of silver ions accelerated the corrosion of pure iron matrix and exhibited a uniform corrosion behavior. However, the shallow depth of ion implantation (~60 nm) only provided those desirable effects on the thin surface and for a short period. Liu et al [15] developed a Fe-30Mn-1Ag alloy using a rapid solidification technique and found that the alloy corroded faster in simulated body fluid due to the microgalvanic effect of the Ag-rich particles with the Fe-Mn matrix. Similar microgalvanic effect of silver addition to accelerating corrosion was observed by Wiesner et al [16] on Fe-Mn-Ag alloys prepared by selective laser melting from mixed powders of Fe-Mn and Ag. However, at longer immersion period, they observed the formation of oxide/phosphate-based corrosion layer that inhibited the microgalvanic effect to

take place. Therefore, silver addition alone seems ineffective for accelerating corrosion of iron-based metals.

Aside from alloying, grain size also affects the corrosion behavior of metals. Gollapudi [17] developed a mathematical model that relates corrosion current density to the grain size of pure metals (Eq. 1). In this model, corrosion medium determines corrosion rate where active medium increases the rate (+b) and passive medium reduces it (-b). Grain refinement in the active medium leads to an increase of current density [18], however when the medium shifts into the passive region, a passive oxide film is formed [17].

$$i_{corr} = a + bd^{-\frac{1}{2}} \quad (1)$$

Where, a and b are constant of the metal and d is the grain size (µm). Obayi et al [19] reported that grain refinement of pure iron via bi-directional rolling leads to a uniform surface corrosion but without significant change on corrosion rate when compared to that of uni-directional rolling. Hence, grain refinement alone seems to be ineffective to accelerate corrosion of iron-based metals.

A structure that combines fine and coarse grains (bimodal structure) could be an interesting alternative to control the corrosion rate [20, 21]. Moreover, this structure can provide both high strength and ductility, which are desirable for stent applications. Mechanical alloying is a method to produce fine grain biodegradable Fe-based [22] and Zn-based [23] metals. Srinivasarao et al [24] produced a bimodal structure of ferrite steel composed of fine grains (<100 nm) and micrometer grains via mechanical alloying and Spark Plasma Sintering (SPS) process. The steel possessed an optimal strength and ductility of 1500 MPa and 15%, respectively. This combination of high strength and ductility in bimodal ferrite steel could be related to the fine-grained strengthening, back-stress strengthening, and precipitation strengthening [20]. The SPS allows a rapid sintering process (i.e. very high heating/cooling rate) thus, it is ideal for preparing nano- and bimodal-structured iron-based metals. Therefore, this study aims mainly to combine silver addition and bimodal structure as a way to accelerate corrosion of iron-based metals. Mechanical alloying and SPS were utilized to produce a set of Fe-30Mn-(1-3)Ag alloys with three different microstructures (i.e. nano, macro and bimodal). Their corrosion behavior was

examined by electrochemical and immersion methods in Hanks' solution at 37 ^{o}C and their mechanical properties were tested by micro-hardness and shear punch test.

2. Materials and Methods

2.1. Samples preparation and characterization

Powders of iron (particle size of 10 µm, 99.5% purity, MerckMillipore, USA), manganese (particle size <100 µm (90%), 99.0% purity, MerckMillipore, USA) and silver (particle size of 2-3.5 µm, 99.9% purity, Sigma-Aldrich, USA) were used. The powders were mixed and milled in a high-energy planetary ball mill (NARYA MPM-2 * 250 H mode, Amin Asia Fanavar Pars, Iran) for 10 h at a rotation speed of 250 rpm and ball-to-powder weight ratio of 30:1. The powder composition was adjusted to produce samples of nanostructured pure iron (NSFe), Fe-30Mn (NS0A), Fe-30Mn-1Ag (NS1A) and Fe-30Mn-3Ag (NS3A) alloys (all in wt. %). Additional micro- (MS1A) and bimodal-structured (BM1A) samples of Fe-30Mn-1Ag were produced from unmilled powders and a mixture of 50% milled with 50% unmilled powders, respectively. The 1 wt.% Ag composition was selected based on the optimum cytotoxicity and antibacterial activity of Fe-30Mn-1Ag alloy proven in our previous study [25]. The chemical composition of the powders after mechanical alloying was measured by using carbon-sulfur analyzer (CS744 Leco, USA) and atomic absorption spectrophotometer (AAnalyst 100, Perkin Elmer, USA).

All powder compositions were consolidated by using SPS technique (EF-20T-10, Easyfashion Changsha, China) at 1000 ºC in a graphite die with a heating rate of 50 ºC/min, holding time of 5 min and pressure of 40 MPa. Particle size and its distribution of consolidated samples were measured by using ImageJ software from at least three different images captured from each specimen. Density of the samples was measured by using helium pycnometer (AccuPyc II 1340 Pycnometer, USA) which is based on measuring the volume of the specimen by gas displacement. The density was calculated from the measured volume and mass.

Microstructural observation was done by using Scanning Electron Microscope (SEM, Quanta 250 FEI, USA) and Transmission Electron Microscope (TEM, EM900 Carl Zeiss, USA) on mechanically polished samples and etched in 1% Nital solution. For bulk TEM preparation, disk shape specimens were ground by using micrometer polishing (grit #800 and #1200) to reduce the

bulk thickness to 500 µm. To decrease the thickness to 100 µm, grinding and polishing were performed by using grit #2400 paper followed by 3 µm and 1 µm diamond solution (Leco, USA). The disks were then dimpled (Dimple grinder II, 657-Gatan, USA) to decrease the thickness of the disk center to 70 µm. Finally, argon ion milling was performed by low angle milling machine (PicoMill Model 1080, Fischione Instruments, USA). Phase analysis was done using an X-ray Diffractometer (XRD, Philips X'Pert Pro, USA) with Cu Kα radiation at scanning angle of 10-90^{o} and a scan rate of 2^{o}/min).

2.2. Corrosion testing

Corrosion behavior of the alloys was studied by means of electrochemical and by immersion test methods. The corrosion media was Hanks' solution prepared by dissolving a prepacked of Hanks' balanced salts (H2387, Sigma-Aldrich, USA) and 0.35 g of sodium bicarbonate (S8875-500G, Sigma-Aldrich, USA) in 1 L of nanopure water which was kept at 37±0.5 ºC throughout the corrosion tests. The initial pH of Hanks' solution was adjusted to 7.4±0.1 and monitored with a pH meter (Accumet pH meter 25, Fisher Scientific, USA). The electrochemical corrosion test was done using a potentiostat (VersaSTAT 3, Princeton Applied Research, USA) with three-electrode system. The samples having exposed surface area of 0.096 cm² served as the working electrode, graphite rod as the counter electrode and saturated calomel as the reference electrode. The test was started by recording the open circuit potential (OCP) for 1 h followed by running the electrochemical impedance spectroscopy (EIS) at a frequency range from 10 kHz down to 0.01 Hz with a sinusoidal potential perturbation of 10 mV rms. Potentiodynamic polarization (PDP) test was then run after the EIS at a scan rate of 0.166 mV/s from -0.25 V to +0.6 V of OCP. All tests were done for three times and analyzed by the VersaStudio software (Princeton Applied Research, USA). ZSimpWin 3.21 software (AMETEK, USA) was used to analyze the EIS results and develop equivalent circuits. Corrosion rate in (mm/year) was calculated from the PDP results based on the ASTM G59 using Eq. 2 [26]:

$$CR = 3.27\times10^{3}\,\frac{i_{corr}\,EW}{\rho} \qquad (2)$$

Where, EW is equivalent weight based on oxidation of Fe to Fe^{2+} and considered to be 27.92 (g/eq). ρ is density (g/cm^3) and it is calculated as follows: 7.74 (Fe-30Mn), 7.76 (Fe-30Mn-1Ag), 7.78 (Fe-30Mn-3Ag) g/cm^3.

Immersion tests were carried out in the Hanks' solution following the ASTM G31 standard [27] for the duration of 14 days on specimens having 15 mm diameter and 1.4 mm thickness. Corrosion rate was calculated based on mass loss by using Eq. 3:

$$CR = 8.76 \times 10^4 \frac{M}{At\rho} \quad (3)$$

Where, t is the test duration (h), A is the surface area of the sample (cm^2) and M is the mass loss amount (g). Finally, surface morphology and chemical analysis of the corroded samples were analyzed using the SEM/EDS.

2.3. Mechanical testing

Hardness test was done on polished samples using a Vickers micro-hardness tester (MMT-X7A, Matsuzawa, Japan) with load of 50 g for 13 s. Average hardness value was obtained from ten measurements. Mechanical properties, i.e. shear strength, of the alloys were evaluated via shear punch test using a 20 kN universal testing machine (STM20, Santam, Tehran, Iran). Detail description of the test procedure is published elsewhere [28]. Briefly, specimens of 15 mm diameter and 0.7-0.8 mm thickness were ground with grit #600 paper and punched using a 3.1 mm diameter punch at a cross-head speed of 0.25 mm/min. The test was repeated for three times.

3. Results and Discussion

3.1. Microstructural observation and phase analysis

Initially, the powder size was as large as 100-200 µm for manganese and 10-50 µm for iron (Fig. 1a). After 10 h of milling, a finer iron powder of 2-10 µm was obtained (Fig. 1b) and agglomerated iron/manganese powders of 10-70 µm were formed (Fig. 1c) from very fine powders of less than 2 µm (inset). All these powders were used to prepare the nanostructured samples (NSFe, NS1A, NS3A), while the bimodal structured sample (BM1A) was prepared from the mixture of initial and milled powders. In order to verify the purity of milled powders, chemical composition of the mechanically alloyed Fe-30Mn-1Ag was determined and presented in Table 1. Some impurities were detected at very low level including carbon and sulfur which may segregate in grain boundary and might affect corrosion resistance and mechanical strength of the alloy [29]. The presence of phosphorous and tin may also increase corrosion rate.

However, the precise effect of each element to corrosion is not within the scope of the present work.

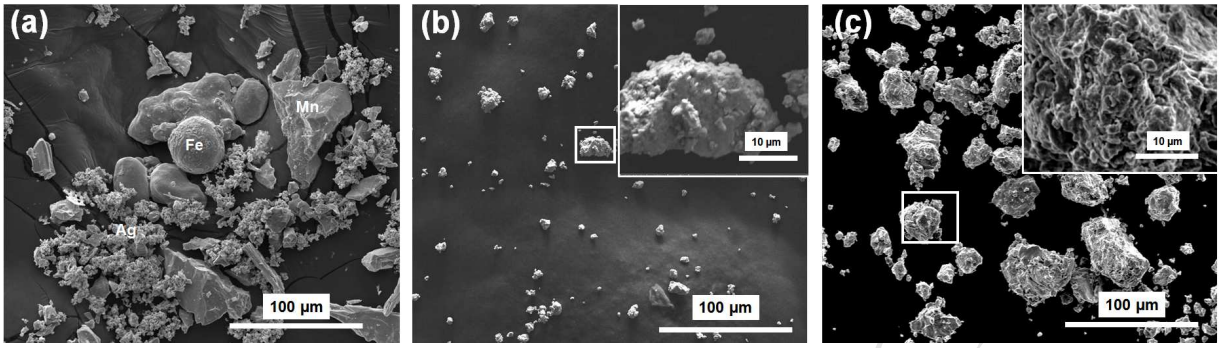

Fig. 1. SEM images showing the morphology of: (a) mixture of Fe-Mn-Ag powders before milling, (b) pure iron powders after 10 h milling, (c) mixture of Fe/Mn/Ag powders after 10 h milling.

Table 1. Chemical composition of Fe-30Mn-1Ag after mechanical alloying

Element	C	Mn	Cu	Ag	S	Sn	P	Si	Al	Ni	Cr	Fe
Wt. %	0.009	30.2	0.017	1.14	0.004	0.014	0.009	0.04	0.005	0.04	0.05	Bal.

After the SPS consolidation, the NSFe sample shows a very fine microstructure (Fig. 2a) which is in contrast with that of NS0A that has coarser grains (Fig. 2b). Pores are observed in the latter as showed by white arrows. Higher relative density was obtained for the NSFe (98±1%) compared to that of NS0A (92±2%). The finer starting powders led to finer grains of NSFe sample (4-8 µm) compared to the NS1A and NS3A alloys. Finer powders also led to smaller pores in NSFe which were eliminated quickly during sintering, while the larger pores formed between agglomerate powders in NS0A and NS1A were more resistant to sintering densification [30]. The manganese powders added thermal inhomogeneity during sintering and cooling resulting in different contraction. Addition of silver reduced the grain size and porosity as observed on NS1A (1 wt.% Ag, Fig. 2c) and its effect is more pronounced on NS3A (3 wt.% Ag, Fig. 2d). The addition of silver helped the SPS consolidation by promoting liquid phase sintering [31]. The melted silver pulled metal particles together and thus reduce pore formation [32] resulting in the increase of relative density to 93±2 % for the NS1A. As the result of coarse starting powders, the MS1A microstructure has obviously coarse grains (Fig. 2e), while the

BM1A consists of coarse and fine grains (Fig. 2f). Comparing Fig. 2g and 2h reveals the position of iron and manganese and shows that silver are distributed uniformly in BM1A, although with some agglomerations (Fig. 2i). The mixture of fine and coarse powders during the SPS consolidation of the BM1A increased relative density to 98±1% from 97±2% of the MS1A.

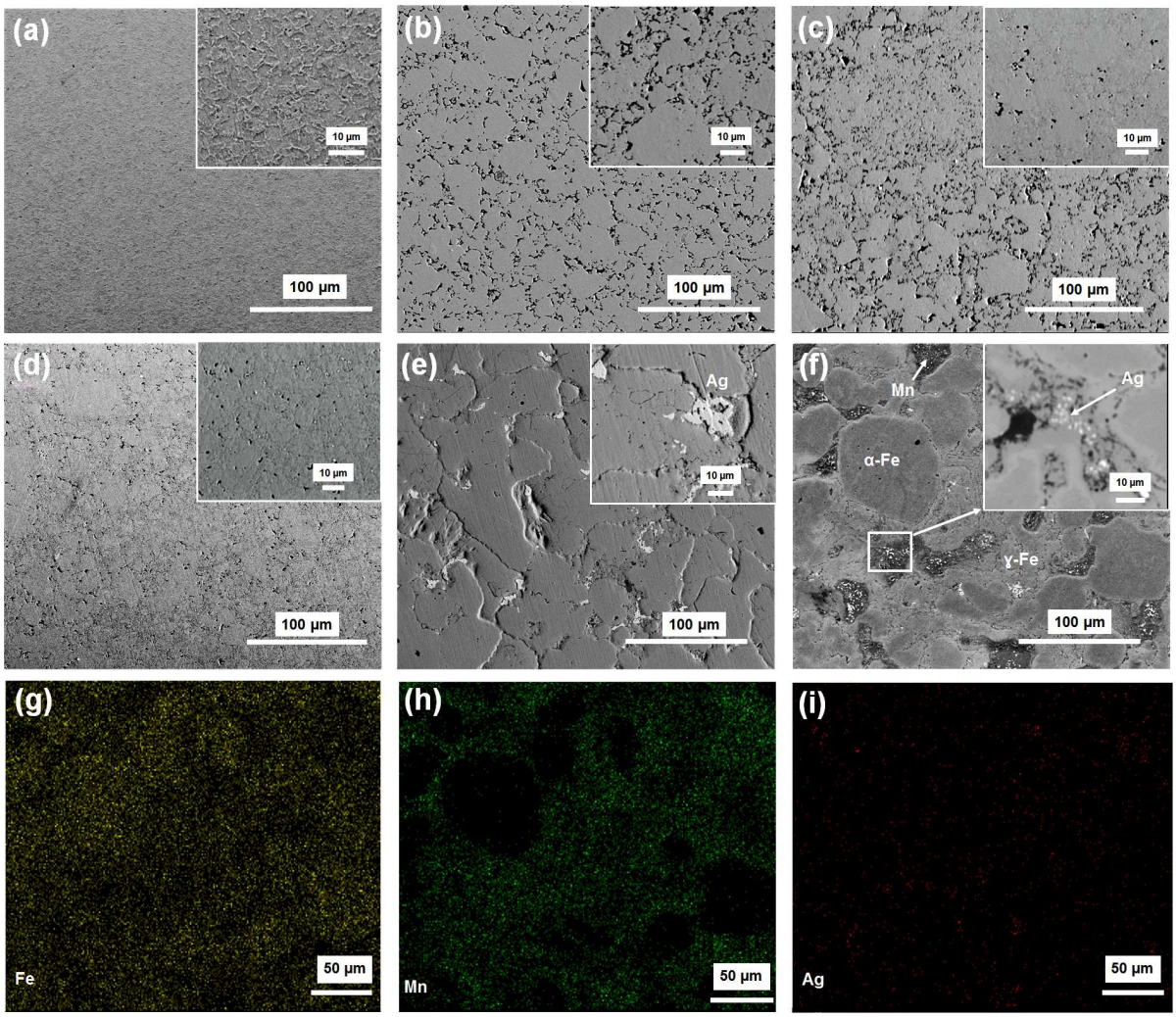

Fig. 2. SEM images showing the microstructure of: (a) NSFe, (b) NS0A, (c) NS1A, (d) NS3A, (e) MS1A, (f) BM1A after the SPS consolidation; and EDS elemental maps of BM1A for: (g) iron, (h) manganese and (i) silver.

The nano-structured samples (NSFe, NS0A, NS1A and NS3A) are characterized with fine consolidated powders, hence called particles, sized between 4 to 6 µm (Fig. 3a-d). The MS1A

and BM1A possess a higher average particle size (Fig. 3e, 3f) which is in agreement with the powder size shown in Fig. 2e and 2f. Two size distributions are found for BM1A which correspond to milled and umilled particles. The size of milled and umilled particles in BM1A could be estimated from that of NS1A and MS1A which is around 4±2 µm and 29±13 µm, respectively. However, there could be some restriction to unmilled particles during sintering by milled particles which could decrease the grain growth in BM1A (23±19 µm).

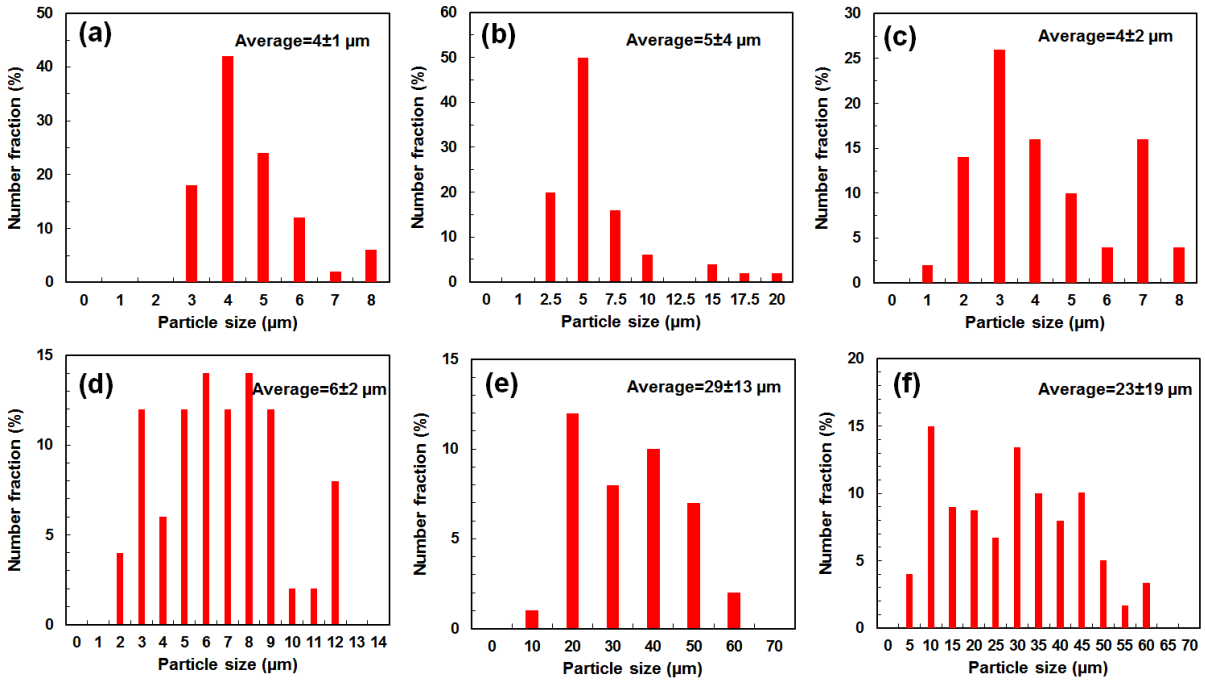

Fig. 3. Particle size distribution of consolidated samples: (a) NSFe, (b) NS0A, (c) NS1A, (d) NS3A, (e) MS1A and (f) BM1A.

After the SPS consolidation, γ-FeMn phase was formed in all samples having 30 wt.% manganese (NS0A, NS1A, NS3A) while the NSFe, MS1A, and BM1A were composed of α-Fe, α-Fe+α-Mn, γ-FeMn+α-Fe+α-Mn, respectively (Fig. 4a, 4b). In NS1A, a complete solid solution formed during 10 h of mechanical alloying [25]. While 100% of MS1A and 50% of BM1A were composed of unmilled powders of α-Fe, α-Mn and silver. There exists a negligible minor amount of MnO formed due to the high reactivity of manganese with oxygen. The presence of α-Mn indicates that the short period of SPS consolidation did not allow a complete formation of solid solution in the coarse particles of MS1A and BM1A.

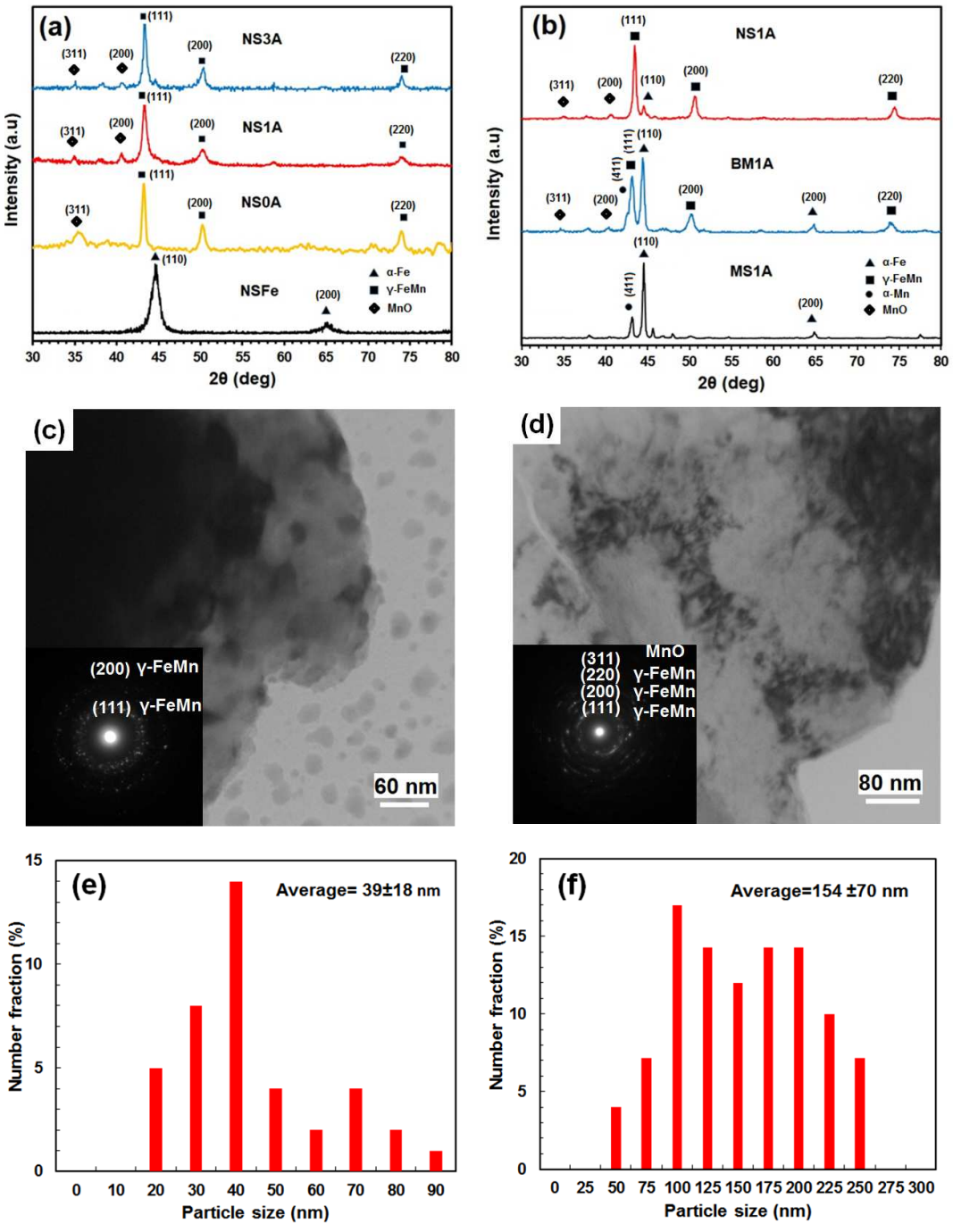

Fig. 4. XRD patterns of different consolidated samples (a, b), TEM bright-field images and SAD pattern of (c) 10 h milled powders and (d) consolidated NS1A samples, and crystallite size distribution of (e) 10 h milled powders and (f) consolidated NS1A samples.

Crystallite size of the samples was calculated from the XRD patterns using Williamson-Hall method [33] and presented in Table 2 alongside with the results from the micro-hardness test. Alloying with manganese increased crystallite size from 96 nm of NSFe to 179 nm of NS0A, while the addition of silver further decreases the crystallite size of Fe-Mn alloy from 150 nm of NS1A to 129 nm of NS3A. TEM image was used to further evaluate and compare the crystallite size obtained from the XRD patterns. As confirmed by TEM bright-field images (Fig. 4c, 4d) and related crystallite size distribution (Fig. 4e, 4f), the average crystallite size of NS1A sample is slightly bigger than that of the 10 h milled powders, indicating a small crystal growth due to rapid sintering process [34]. The grain growth was probably inhibited by the segregated silver in the grain boundaries due to its negligible solubility in both iron and manganese [35, 36].

Table 2. Phase, crystallite size, and micro-hardness of the consolidated samples

Sample	Phase	Crystallite size (nm)	Micro-hardness (Hv)
NSFe	α-Fe	96	223 ± 15
NS0A	γ-FeMn	179	464 ± 19
NS1A	γ-FeMn	150	483 ± 18
NS3A	γ-FeMn	129	511 ± 25
MS1A	α-Fe	490	88 ± 21
	α-Mn	630	894 ± 56
BM1A	α-Fe	450	96 ± 11
	γ-FeMn	155	472 ± 34
	α-Mn	641	933 ± 75

Alloying with manganese increased the micro-hardness of the samples from 223 Hv for NSFe to 464 Hv for NS0A (Table 2). While the addition of silver increased the hardness slightly from 483 Hv for NS1A to 511 Hv for NS3A. The macro- and bimodal-structured samples (MS1A and BM1A) were composed of multiphase with different micro-hardness. This difference could provide a composite effect between the softer phase (α-Fe) and harder phases (γ-FeMn and α-Mn). Generally, fully ferritic low carbon steels show high elongation [37]. While manganese twinning induced plasticity (TWIP) [38] and transformation induced plasticity (TRIP) [39] steels possess a good strength and ductility due to combination of α-Fe and γ-Fe phases.

3.2. Corrosion behavior and effect of silver addition and microstructure

Alloying with manganese decreased the open circuit and corrosion potentials of iron, while the addition of silver did not show a notable change (Fig. 5a, b). However, silver addition increased corrosion current density of the Fe-Mn alloys as extrapolated by Tafel fitting from the polarization curves (Fig. 5b). The current density increases from 18.7 µA/cm^2 for NS0A to 25.3 and 44.8 µA/cm^2 for NS1A and NS3A, respectively (Table 3). Consequently, corrosion rate increased from 0.24 mm/year for NS0A to 0.33 and 0.58 mm/year for NS1A and NS3A, respectively. As manganese shifts the free corrosion potential to the less noble values, alloying with iron increases the corrosion rate [40]. Silver addition was found to form Ag-rich particles within the Fe-Mn matrix that gives a microgalvanic effect thus accelerating corrosion [15, 16].

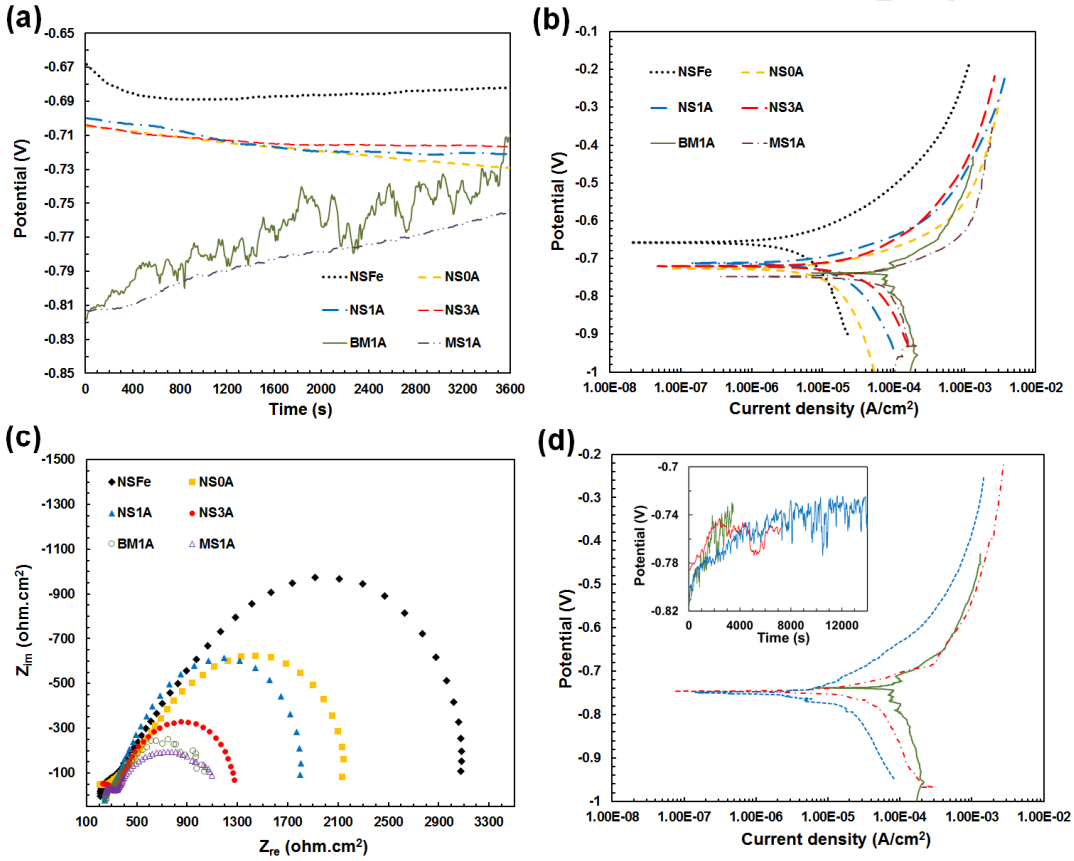

Fig. 5. Electrochemical test results of all samples: (a) open circuit potential, (b) potentiodynamic polarization, (c) Nyquist plots, (d) potentiodynamic polarization after prolonged OCP for BM1A sample.

As compared to the nanostructured NS1A sample, the microstructured MS1A and bimodal structured BM1A shows more negative open circuit potential (Fig. 5a), but with unstable behavior for the latter. The microgalvanic coupling between α-Fe and γ-FeMn phases, in addition to Ag-rich particles, seems to play a role in this behavior. This, in turn, resulted into a higher corrosion current density of BM1A (75.9 µA/cm^2) compared to that of MS1A (68.5 µA/cm^2) and NS1A (25.3 µA/cm^2) as extrapolated from the polarization curves (Fig. 5b). The corrosion rate of BM1A is about three times higher than the NS1A, 0.88 mm/year vs 0.33 mm/year. In a study on super duplex stainless steel, Lee et al [41] showed that corrosion current density depended on the existing phases. Polarization resistance of γ-Fe was higher than that of α-Fe. This may explain that the presence of α-Fe and γ-FeMn in BM1A formed a microgalvanic cells that accelerated corrosion. In addition, a study on a bimodal structure of 7075 aluminum alloy found that coarse grains have a higher dissolution rate in NaCl solution which was related to the electrochemical heterogeneity of the mixed grain size [42]. Dehestani et al [43] found higher corrosion rate for Fe-30Mn alloy when using coarse iron particle in contrast to super fine one. Micro-galvanic, preferential and localized corrosion attributed to varying manganese concentration between sintered particles. Although this preferential localized corrosion improves the overall corrosion rate, it brings a concern over possible detrimental effects on a device stability and lead to an early device failure that needs to be addressed in the future.

Table 3. Corrosion parameters derived from PDP and EIS results

Sample	PDP parameter		EIS parameter			
	Current density (µA/cm^2)	Corrosion rate (mm/year)	R_1 (ohm)	R_2 (ohm)	Q_1 (µF)	Q_2 (µF)
NSFe	7.7 ± 1	0.1 ± 0.02	2977 ± 238	256.3 ± 20	7.15 ± 0.5	26 ± 2
NS0A	18.7 ± 2	0.24 ± 0.02	1784 ± 142	337 ± 27	45.18 ± 3	15.38 ± 1
NS1A	25.3 ± 2	0.33 ± 0.02	1534 ± 122	157.1 ± 12	49.29 ± 4	5.07 ± 0.4
NS3A	44.8 ± 3	0.58 ± 0.04	1002 ± 80	70.9 ± 5	108 ± 8	1.42 ± 0.1
BM1A	75.9 ± 6	0.88 ± 0.07	883 ± 70	77.26 ± 6	472 ± 37	0.32 ± 0.1
MS1A	68.5 ± 5	0.79 ± 0.06	902.5 ± 72	74.1 ± 6	433 ± 34	0.67 ± 0.1

Silver addition tends to decrease the surface impedance of the alloy as shown by decreasing diameter of the Nyquist plots of the silver-containing alloys (Fig. 5c). The impedance behavior of the alloys can be electrically modeled as a porous layer (Table 3). R_s represents Hanks' solution resistance between the alloy sample and the reference electrode that is 225±25 ohm, while R and Q is electrical resistance and capacitance of the corrosion layer, respectively. Charge transfer process at the interface of porous film and electrolyte is shown by R1Q1. R1 and Q1 is electrical resistance and capacity of the porous oxide film, respectively. At the interface of the pore and the sample, parallel combination of R2Q2 correspond to the impedance and the pore resistance. Here, increasing silver decreased R1 and R2 and it is in accordance to higher corrosion rate that was measured by PDPs. Also, values of R1, R2 of BM1 and MS1 are close to each other and lower than NS1A. Lakatos-Varsányi et al [44] observed that during immersion of a silver coated titanium alloy the electrolyte gradually penetrates into the substrate in silver coated areas. As an OCP stability did not reach by the BM1A sample even at a prolonged OCP test up to 4 h (Fig. 5d), an EIS analysis became difficult to perform. The reactivity of the samples did not provide a steady-state condition that is required for a successful EIS experiment [45]. Hence, PDPs were conducted after longer stabilization time. Corrosion current density and corrosion rate decreased by increasing stabilization time from 75.9 $\mu A/cm^2$ and 0.88 mm/year after 1 h to 15.4 $\mu A/cm^2$ and 0.21 mm/year after 4 h. The heterogenic phase mixture and bimodal grain size of BM1A (Fig. 2f) helped to increase the corrosion rate. However, further investigation should be performed to differentiate between the effects of these two factors on the corrosion rate.

3.3. Corrosion layer characterization and its evolution

After subjected to polarization, corrosion product formed on the surface of the alloys with a seemingly denser layer on NSFe and NS0A (Fig. 6a, 6b) than those of NS1A and NS3A (Fig. 6c, 6d). While corrosion layer on MS1A (Fig. 6e) seems denser than that of NS1A and BM1A. As detected by the EDS, aside of iron, manganese, and oxygen, corrosion product on the surface of NS0A and NS1A contained similar amount of phosphorous, but with the presence of calcium in the former (Table 4). Iron and manganese oxides formed on the MS1A surface in a spherical shape, without other detected element. The surface composition of BM1A is similar to that of NS1A except that low amount of chloride and calcium was detected on the former. Differently,

high amount of chloride was detected on the corrosion product on NS3A surface. Chloride ions in the Hanks' solution should have been reacted with the silver and formed a rather porous corrosion layer, which also explains the decrease in impedance from NS0A to NS3A. A more pronounce effect of chloride ions took place on BM1A surface, which may explain the high corrosion rate of this alloy.

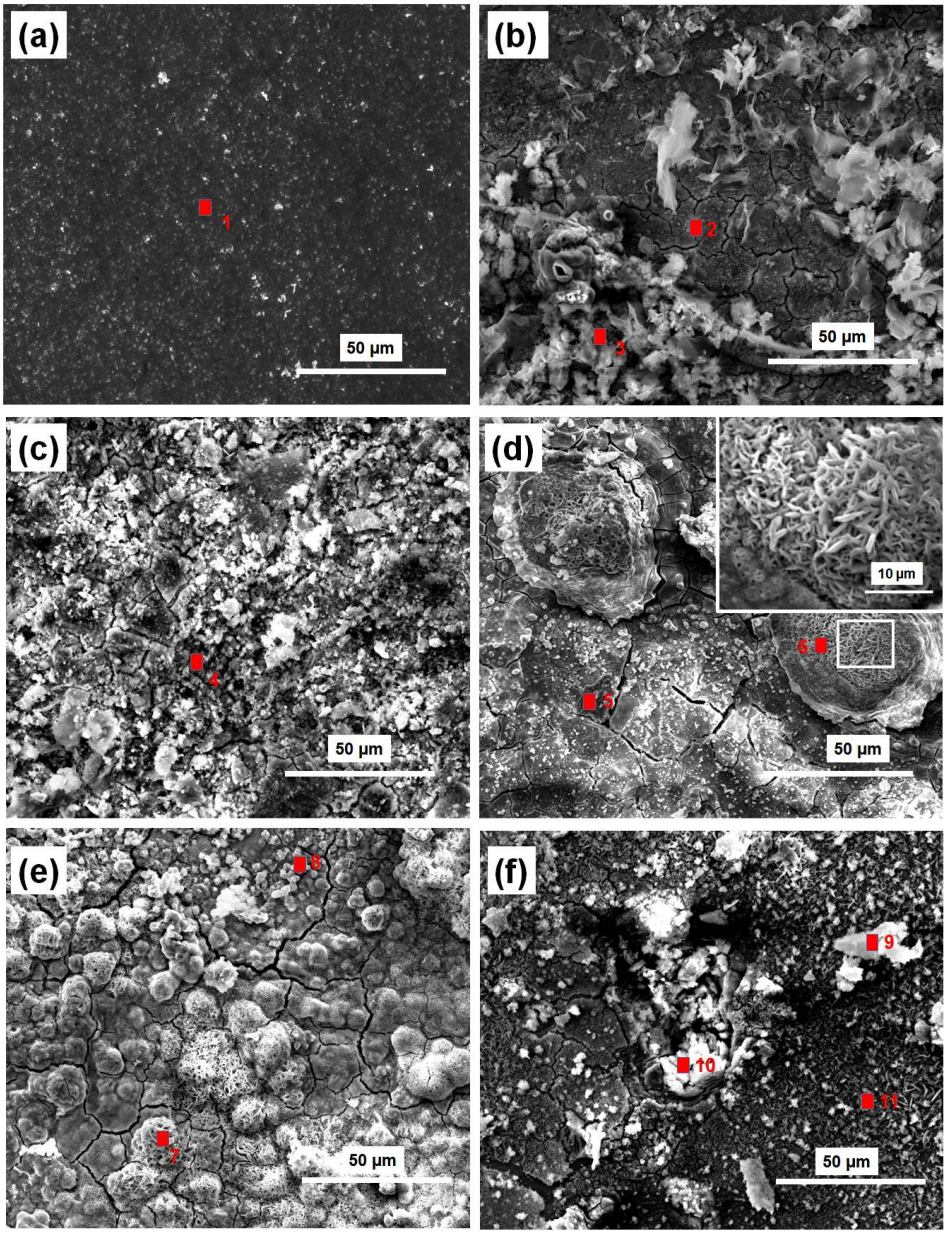

Fig. 6. SEM micrographs of the alloys' surface after subjected to polarization test: (a) NSFe, (b) NS0A, (c) NS1A, (d) NS3A, (e) MS1A, and (f) BM1A.

Table 4. Chemical composition of points indicated in Fig. 6 and Fig. 7 as measured by the EDS

	Elements (wt. %)						
Point	Fe	Mn	Ag	O	Cl	P	Ca
1	89.65	-	-	10.35	-	-	-
2	43.89	18.73	-	37.38	-	-	-
3	59.05	21.64	-	14.77	-	1.64	2.9
4	35.95	17.99	-	44.33	-	1.99	-
5	20.19	36.13	-	39.53	4.14	-	-
6	28.42	18.47	-	33.89	19.22	-	-
7	33.6	22.49	-	43.91	-	-	-
8	46.83	10.67	-	42.5	-	-	-
9	35.94	15.98	-	43.89	1.36	2.83	-
10	13.29	32.35	-	47.22	2.13	2.63	2.39
11	68.22	1.71	-	30.07	-	-	-
12	33.86	12.51	1.13	39.64	1.15	4.39	7.33
13	11.5	50.19	-	34.42	-	3.9	-
14	44.1	18.33	-	32.85	1.36	4.71	-
15	54.57	17.12	-	20.22	-	3.14	4.95

Evolution of the corrosion layer over time was observed for MS1A, BM1A and NS1A samples (Fig. 7). As mentioned earlier the BM1A showed an OCP instability during 1 and 4 h immersion in Hanks' solution (Fig. 5d). Over time, chloride, phosphorous and calcium precipitated on the alloy's surface and calcium phosphate may have been formed. The low content of chloride may indicate that AgCl, as well as FeCl and MnCl, are soluble [16]. Differently, Fe-Mn oxides/phosphates have low solubility, thus precipitated on the surface and inhibit the microgalvanic effect of Ag-rich particle and the Fe-Mn matrix as has been confirmed by Wiesener et al using Raman imaging [16]. The Fe-Mn oxides/phosphates formed flower-like precipitates that grew over the time of immersion (Fig. 7b, 7c).

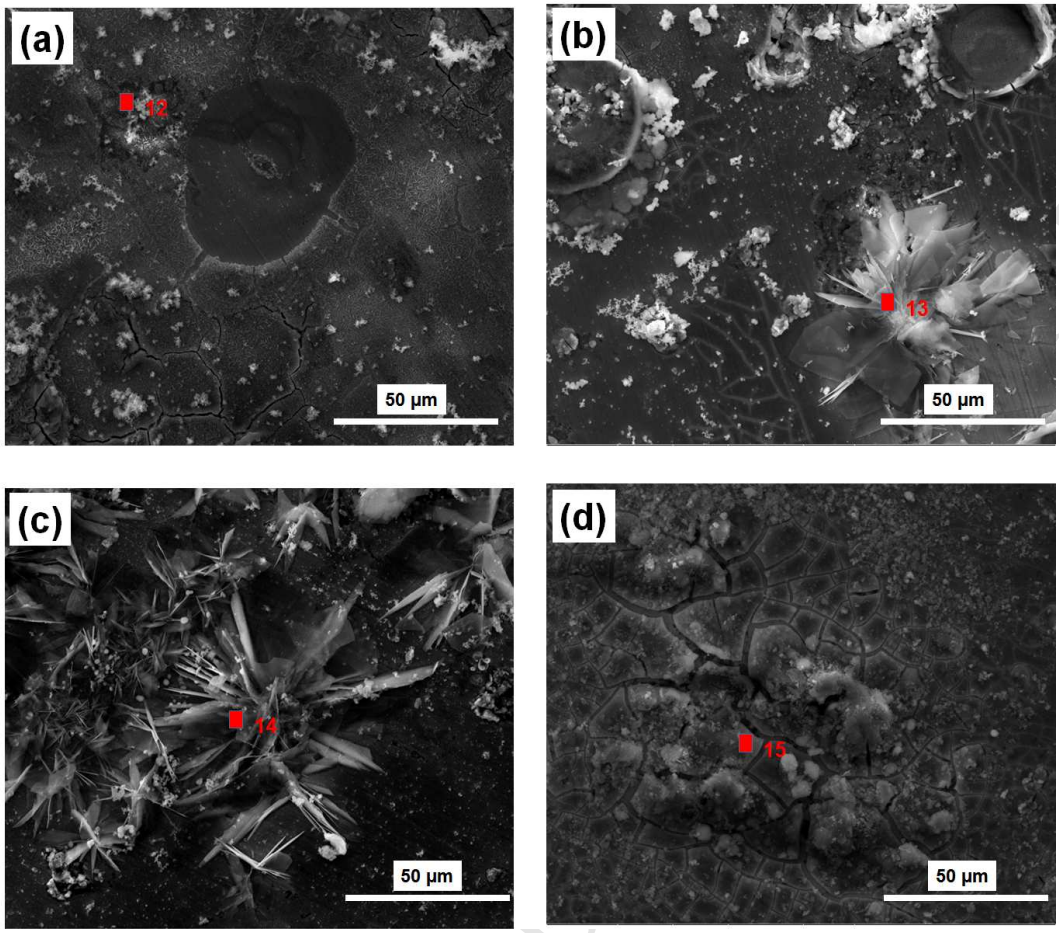

Fig. 7. SEM micrographs of the alloy's surface after subjected open circuit potential test at different period: (a) MS1A for 1 h, (b) BM1A for 1 h, (c) BM1A for 4 h, and (d) NS1A for 1 h (point analysis are in Table 4).

As PDP is an accelerated corrosion test, static immersion test was performed for a longer period of 15 days in Hanks' solution for NS1A, BM1A and MS1A samples. The results (Fig. 8a) show that mass loss increased sharply after 7 days, then it increased gradually after 14 days. The corrosion rates of the alloys were calculated to be 0.07, 0.14 and 0.12 mm/year for NS1A, BM1A and MS1A, respectively. While, the corrosion rates of the NS1A, BM1A and MS1A are 0.33, 0.88 and 0.79 mm/year, respectively. There is a difference between the corrosion rates obtained from PDP test and those calculated from immersion test. However, both results show a similar trend indicating that BM1A (bimodal structured alloy) corrodes faster than NS1A (nanostructured alloy) and MS1A (macrostructured alloy).

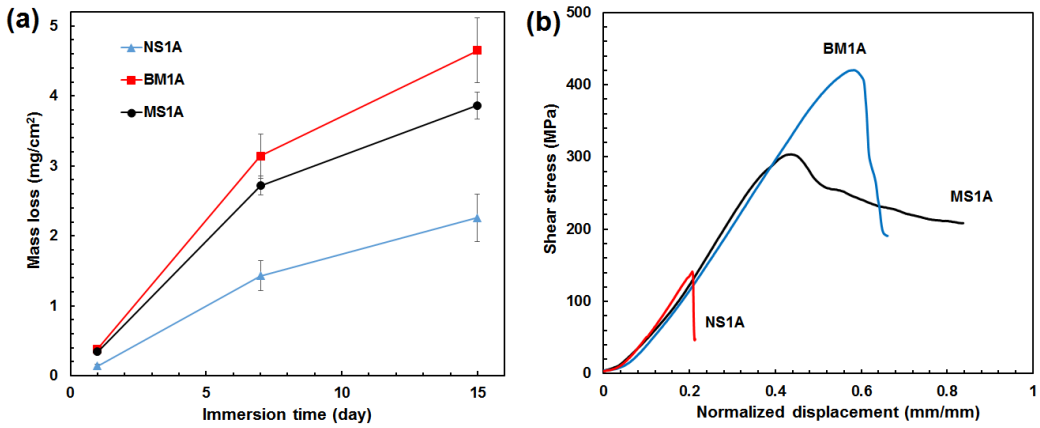

Fig. 8. (a) Static degradation rate of NS1A, BM1A, and MS1A, and (b) shear stress vs. normalized punch displacement of NS1A, BM1A, and MS1A samples.

Table 5. Mechanical properties of NS1A, BM1A, and MS1A

Sample	Shear yield strength (MPa)	Shear ultimate strength (MPa)	Shear strain (mm/mm)
NS1A	-	139.79 ± 10	0.29 ± 0.01
BM1A	361.5 ± 22	420.28 ± 35	0.74 ± 0.02
MS1A	277.84 ± 13	303.37 ± 15	0.95 ± 0.05

To predict the mechanical properties of the alloys, a small specimen shear punch test was performed as used by Guduru et al [46]. The results showed that the NS1A and MS1A samples have a shear strength of 139.79±10, and 303.37±15 MPa, respectively (Fig. 8b and Table 5). The presence of pores and crystal defects in NS1A matrix and its high hardness could be the reason for the low strength and strain [47]. Mahesh et al [48] reported that nanocrystalline Fe-Cr powder exhibited a difficult plastic deformation due to its high hardness. However, the combination of nano- and microstructure in BM1A resulted into a high shear stress and shear strain (420.28±35 MPa and 0.74±0.02 mm/mm). The micron-sized grain of BM1A improved the alloy's ductility due to a higher dislocation storage capacity and consequently higher work hardening capability when compared to nano-sized grain [49]. Based on Von-Mises yield criterion if there is pure shear applying to the specimen there would be a correlation between tensile (σ) and shear stress (τ) as $\sigma = \sqrt{3}\tau$ [50], hence the tensile strengths of NS1A, BM1A, and MS1A are equivalent to

244, 722 and 522 MPa, respectively. The results are in agreement to Von-Mises yield criterion for different materials evaluated both with shear punch test and tensile test [51, 52]. Using the same criteria it is possible to estimate the tensile strain (ε) from the shear strain (γ), which gives $\varepsilon = \left(1/\sqrt{3}\right)\gamma$. So, the tensile strain of NS1A, BM1A and MS1A samples are equivalent to 0.12, 0.38 and 0.48 mm/mm, respectively. The results are comparable to Fe–Cr–Ni–Zr bimodal alloy with the ultimate shear stress of 778 MPa and shear strain of 0.44 [48], while our approach eliminated incorporating alloying elements such as Ni and Zr. The ultimate tensile strength and strain enhancement by bimodal structure also surpass other Fe-based alloys such as annealed 316L stainless steel (586 MPa) [53], mechanically alloyed Fe–Mn-Si by (350 MPa) [54], sintered and cold rolled Fe-35Mn (550 MPa and 0.31 mm/mm) [55], nitrided Fe (614 MPa) [9], TWIP steel Fe-Mn-C-S (772 MPa and 0.3 mm/mm) [6], respectively.

4. Conclusion

The low corrosion rate problem of iron-based biodegradable alloys has been addressed in this study by combining noble element addition and forming the bimodal structure of Fe-30Mn-1Ag alloys via mechanical alloying and spark plasma sintering process. The addition of silver up to 3 wt.% increases relative density of the alloy due to liquid phase sintering. Most of the silver precipitated in the grain boundaries and results into minimizing grain growth and forming microgalvanic sites that accelerate corrosion. A γ-FeMn phase is formed in nanostructured Fe-30Mn-1Ag, a combination of α-Fe+α-Mn is formed in macrostructured Fe-30Mn-1Ag, and γ-FeMn+α-Fe+α-Mn is formed in bimodal-structured Fe-30Mn-1Ag. The optimum mechanical properties were obtained for the bimodal-structured Fe-30Mn-1Ag alloy having an equivalent tensile strength and strain of 722 MPa and 0.38 mm/mm, respectively. The bimodal Fe-30Mn-1Ag corrodes at 0.88 mm/year which is faster than the same alloys in nanostructured (0.33 mm/year) and macrostructured condition (0.79 mm/year), as measured by polarization. The immersion test shows similar trend of corrosion rate. The heterogenic phase mixture and bimodal grain size of the bimodal-structured Fe-30Mn-1Ag helps to increase the corrosion rate. However, the effect of each factor need to be further investigated. The preferential microgalvanic localized corrosion improves the overall corrosion rate, but it brings a concern over possible detrimental effects on a device stability that needs to be addressed in the future.

Acknowledgments

The authors acknowledge the financial support of Nanotechnology Initiative Council of Iran [grant number 115844] and Natural Sciences and Engineering Research Council of Canada (NSERC). Pedram Sotoudeh Bagha thanks the Ministry of Science, Research and Technology of Iran for sponsoring his research visit at the CHU de Québec Research Center, Laval University, Prof. Diego Mantovani (Canada Research Chair in Biomaterials and Bioengineering for the Innovation in Surgery) and Prof. Edward Ghali for their support and guidance.

References

[1] H. Hermawan, Updates on the research and development of absorbable metals for biomedical applications, Prog. Biomater. (2018). doi:10.1007/s40204-018-0091-4.

[2] W. Lin, L. Qin, H. Qi, D. Zhang, G. Zhang, R. Gao, et al., Long-term in vivo corrosion behavior, biocompatibility and bioresorption mechanism of a bioresorbable nitrided iron scaffold, Acta Biomater. 54 (2017) 454–468. doi:10.1016/j.actbio.2017.03.020.

[3] T. Kraus, F. Moszner, S. Fischerauer, M. Fiedler, E. Martinelli, J. Eichler, et al., Biodegradable Fe-based alloys for use in osteosynthesis: Outcome of an in vivo study after 52weeks, Acta Biomater. 10 (2014) 3346–3353. doi:10.1016/j.actbio.2014.04.007.

[4] A. Drynda, T. Hassel, F.W. Bach, M. Peuster, In vitro and in vivo corrosion properties of new iron-manganese alloys designed for cardiovascular applications., J. Biomed. Mater. Res. B. Appl. Biomater. 103 (2015) 649–60. doi:10.1002/jbm.b.33234.

[5] J. Čapek, K. Stehlíková, A. Michalcová, Š. Msallamová, D. Vojtěch, Microstructure, mechanical and corrosion properties of biodegradable powder metallurgical Fe-2 wt% X (X = Pd, Ag and C) alloys, Mater. Chem. Phys. 181 (2016) 501–511. doi:10.1016/j.matchemphys.2016.06.087.

[6] J. Hufenbach, H. Wendrock, F. Kochta, U. Kühn, A. Gebert, Novel biodegradable Fe-Mn-C-S alloy with superior mechanical and corrosion properties, Mater. Lett. 186 (2017) 330–333. doi:10.1016/j.matlet.2016.10.037.

[7] T. Huang, J. Cheng, D. Bian, Y. Zheng, Fe-Au and Fe-Ag composites as candidates for biodegradable stent materials., J. Biomed. Mater. Res. B. Appl. Biomater. 104 (2016) 225–40. doi:10.1002/jbm.b.33389.

[8] T. Huang, J. Cheng, Y.F. Zheng, In vitro degradation and biocompatibility of Fe-Pd and Fe-Pt composites fabricated by spark plasma sintering, Mater. Sci. Eng. C. 35 (2014) 43–53. doi:10.1016/j.msec.2013.10.023.

[9] Q. Feng, D. Zhang, C. Xin, X. Liu, W. Lin, W. Zhang, et al., Characterization and in vivo evaluation of a bio-corrodible nitrided iron stent, J. Mater. Sci. Mater. Med. 24 (2013) 713–724. doi:10.1007/s10856-012-4823-z.

[10] T. Huang, Y. Cheng, Y. Zheng, In vitro studies on silver implanted pure iron by metal vapor vacuum arc technique, Colloids Surfaces B Biointerfaces. 142 (2016) 20–29. doi:10.1016/j.colsurfb.2016.01.065.

[11] T. Jurgeleit, E. Quandt, C. Zamponi, Magnetron sputtering a new fabrication method of iron based biodegradable implant materials, Adv. Mater. Sci. Eng. 2015 (2015) 1–9. doi:10.1155/2015/294686.

[12] A.H.M. Yusop, N.M. Daud, H. Nur, M.R.A. Kadir, H. Hermawan, Controlling the degradation kinetics of porous iron by poly(lactic-co-glycolic acid) infiltration for use as temporary medical implants, Sci. Rep. 5 (2015) 11194. doi:10.1038/srep11194.

[13] K. Cysewska, L.F. Macía, P. Jasiński, A. Hubin, Tailoring the electrochemical degradation of iron protected with polypyrrole films for biodegradable cardiovascular stents, Electrochim. Acta. 245 (2017) 327–336. doi:10.1016/j.electacta.2017.05.172.

[14] Y. Qi, H. Qi, Y. He, W. Lin, P. Li, L. Qin, et al., Strategy of metal–polymer composite stent to accelerate biodegradation of iron-based biomaterials, ACS Appl. Mater. Interfaces. 10 (2018) 182–192. doi:10.1021/acsami.7b15206.

[15] R.-Y. Liu, R.-G. He, L.-Q. Xu, S.-F. Guo, Design of Fe–Mn–Ag alloys as potential candidates for biodegradable metals, Acta Metall. Sin. (English Lett. 31 (2018) 584–590. doi:10.1007/s40195-018-0702-z.

[16] M. Wiesener, K. Peters, A. Taube, A. Keller, K.P. Hoyer, T. Niendorf, et al., Corrosion properties of bioresorbable FeMn-Ag alloys prepared by selective laser melting, Mater. Corros. 68 (2017) 1028–1036. doi:10.1002/maco.201709478.

[17] S. Gollapudi, Grain size distribution effects on the corrosion behaviour of materials, Corros. Sci. 62 (2012) 90–94. doi:10.1016/j.corsci.2012.04.040.

[18] K.D. Ralston, N. Birbilis, Effect of grain size on corrosion: A review, Corros. Sci. Sect. 66 (2010) 1–13.

[19] C.S. Obayi, R. Tolouei, C. Paternoster, S. Turgeon, B.A. Okorie, D.O. Obikwelu, et al., Influence of cross-rolling on the micro-texture and biodegradation of pure iron as biodegradable material for medical implants., Acta Biomater. 17 (2015) 68–77. doi:10.1016/j.actbio.2015.01.024.

[20] G. Niu, H. Wu, D. Zhang, N. Gong, D. Tang, Study on microstructure and properties of bimodal structured ultrafine-grained ferrite steel, Metals (Basel). 7 (2017) 316. doi:10.3390/met7080316.

[21] M. Rifai, H. Miyamoto, H. Fujiwara, Effects of Strain energy and grain size on corrosion resistance of ultrafine grained Fe-20%Cr Steels with extremely low C and N fabricated by ECAP, Int. J. Corros. 2015 (2015) 1–9. doi:10.1155/2015/386865.

[22] N. Safaie, M. Khakbiz, S. Sheibani, P. SotoudehBagha, Synthesizing of nanostructured Fe-Mn alloys by mechanical alloying process, Procedia Mater. Sci. 11 (2015) 381–385. doi:10.1016/j.mspro.2015.11.134.

[23] P. Sotoudeh Bagha, S. Khaleghpanah, S. Sheibani, M. Khakbiz, A. Zakeri, Characterization of nanostructured biodegradable Zn-Mn alloy synthesized by mechanical alloying, J. Alloys Compd. 735 (2018) 1319–1327. doi:10.1016/j.jallcom.2017.11.155.

[24] B. Srinivasarao, K. Oh-ishi, T. Ohkubo, K. Hono, Bimodally grained high-strength Fe fabricated by mechanical alloying and spark plasma sintering, Acta Mater. 57 (2009) 3277–3286. doi:10.1016/j.actamat.2009.03.034.

[25] P. Sotoudehbagha, S. Sheibani, M. Khakbiz, S. Ebrahimi-Barough, H. Hermawan, Novel antibacterial biodegradable Fe-Mn-Ag alloys produced by mechanical alloying, Mater. Sci. Eng. C. 88 (2018) 88–94. doi:10.1016/j.msec.2018.03.005.

[26] ASTM G59-97(2014), Standard Test Method for Conducting Potentiodynamic Polarization Resistance Measurements, ASTM International, West Conshohocken, n.d.

[27] ASTM G31-72(2004), Standard Practice for Laboratory Immersion Corrosion Testing of Metals 1, West Conshohocken, PA, 2004. doi:10.1520/G0031-72R04.

[28] R. Alizadeh, R. Mahmudi, A.H.W. Ngan, Y. Huang, T.G. Langdon, Superplasticity of a nano-grained Mg–Gd–Y–Zr alloy processed by high-pressure torsion, Mater. Sci. Eng. A. 651 (2016) 786–794. doi:10.1016/j.msea.2015.10.094.

[29] Z.A. Foroulis, H.H. Uhlig, Effect of impurities in iron on corrosion in acids, J. Electrochem. Soc. 112 (1965) 1177. doi:10.1149/1.2423393.

[30] R.M. German, Coarsening in sintering: Grain shape distribution, grain size distribution, and grain growth kinetics in solid-pore systems, Crit. Rev. Solid State Mater. Sci. 35 (2010) 263–305. doi:10.1080/10408436.2010.525197.

[31] M. Fujino, H. Narusawa, Y. Kuramochi, E. Higurashi, T. Suga, T. Shiratori, et al., Transient liquid-phase sintering using silver and tin powder mixture for die bonding, Jpn. J. Appl. Phys. 55 (2016) 04EC14. doi: 10.7567/JJAP.55.04EC14.

[32] R.M. German, P. Suri, S.J. Park, Review: liquid phase sintering, J. Mater. Sci. 44 (2009) 1–39. doi:10.1007/s10853-008-3008-0.

[33] G.K. Williamson, W.H. Hall, X-ray line broadening from filed aluminium and wolfram, Acta Metall. 1 (1953) 22–31. doi:http://dx.doi.org/10.1016/0001-6160(53)90006-6.

[34] M. Omori, Sintering, consolidation, reaction and crystal growth by the spark plasma system (SPS), Mater. Sci. Eng. A. 287 (2000) 183–188. doi:10.1016/S0921-5093(00)00773-5.

[35] L.J. Swartzendruber, The Ag−Fe (Silver-Iron) system, Bull. Alloy Phase Diagrams. 5 (1984) 560–564. doi:10.1007/BF02868316.

[36] I. Karakaya, W.T. Thompson, The Ag-Mn (Silver-Manganese) system, J. Phase Equilibria. 11 (1990) 480–486. doi:10.1007/BF02898263.

[37] J.R. Davis, ed., Materials Selection and Design, in: Metals Handbook, Second Ed., ASM International, 1998: pp. 153–173.

[38] P. Lan, J. Zhang, Tensile property and microstructure of Fe-22Mn-0.5C TWIP steel, Mater. Sci. Eng. A. 707 (2017) 373–382. doi:10.1016/j.msea.2017.09.061.

[39] Y. Xu, Z. Hu, Y. Zou, X. Tan, D. Han, S. Chen, et al., Effect of two-step intercritical annealing on microstructure and mechanical properties of hot-rolled medium manganese TRIP steel containing δ-ferrite, Mater. Sci. Eng. A. 688 (2017) 40–55. doi:10.1016/j.msea.2017.01.063.

[40] J. Čapek, J. Kubásek, D. Vojtěch, E. Jablonská, J. Lipov, T. Ruml, Microstructural, mechanical, corrosion and cytotoxicity characterization of the hot forged FeMn30(wt.%) alloy, Mater. Sci. Eng. C. 58 (2016) 900–908. doi:10.1016/j.msec.2015.09.049.

[41] J.-S. Lee, K. Fushimi, T. Nakanishi, Y. Hasegawa, Y.-S. Park, Corrosion behaviour of ferrite and austenite phases on super duplex stainless steel in a modified green-death solution, Corros. Sci. 89 (2014) 111–117. doi:10.1016/j.corsci.2014.08.014.

[42] W. Tian, S. Li, J. Liu, M. Yu, Y. Du, Preparation of bimodal grain size 7075 aviation aluminum alloys and their corrosion properties, Chinese J. Aeronaut. 30 (2017) 1777–1788. doi:10.1016/j.cja.2017.06.001.

[43] M. Dehestani, K. Trumble, H. Wang, H. Wang, L.A. Stanciu, Effects of microstructure and heat treatment on mechanical properties and corrosion behavior of powder metallurgy derived Fe–30Mn alloy, Mater. Sci. Eng. A. 703 (2017) 214–226. doi:10.1016/j.msea.2017.07.054.

[44] M. Lakatos-Varsányi, M. Furko, T. Pozman, Electrochemical impedance spectroscopy study on silver coated metallic implants, Electrochim. Acta. 56 (2011) 7787–7795. doi:10.1016/j.electacta.2011.01.072.

[45] M.E. Orazem, B. Tribollet, Electrochemical Impedance Spectroscopy, John Wiley & Sons, Inc., Hoboken, NJ, USA, 2017. doi:10.1002/9781119363682.

[46] R.K. Guduru, A. V. Nagasekhar, R.O. Scattergood, C.C. Koch, K.L. Murty, Thickness and clearance effects in shear punch testing, Adv. Eng. Mater. 9 (2007) 157–160. doi:10.1002/adem.200600255.

[47] J. Čapek, Š. Msallamová, E. Jablonská, J. Lipov, D. Vojtěch, A novel high-strength and highly corrosive biodegradable Fe-Pd alloy: Structural, mechanical and in vitro corrosion and cytotoxicity study, Mater. Sci. Eng. C. 79 (2017) 550–562. doi:10.1016/j.msec.2017.05.100.

[48] B.V. Mahesh, R.K. Singh Raman, R.O. Scattergood, C.C. Koch, Fe-Cr-Ni-Zr alloys with bi-modal grain size distribution: Synthesis, mechanical properties and oxidation resistance, Mater. Sci. Eng. A. 574 (2013) 235–242. doi:10.1016/j.msea.2013.02.049.

[49] Y.M. Wang, E. Ma, Three strategies to achieve uniform tensile deformation in a nanostructured metal, Acta Mater. 52 (2004) 1699–1709. doi:10.1016/j.actamat.2003.12.022.

[50] R. Alizadeh, R. Mahmudi, T.G. Langdon, Superplasticity of a fine-grained Mg–9Gd–4Y–0.4Zr alloy evaluated using shear punch testing, J. Mater. Res. Technol. 3 (2014) 228–232. doi:10.1016/j.jmrt.2014.04.004.

[51] R.K. Guduru, K.A. Darling, R. Kishore, R.O. Scattergood, C.C. Koch, K.L. Murty, Evaluation of mechanical properties using shear – punch testing, 395 (2005) 307–314. doi:10.1016/j.msea.2004.12.048.

[52] R. Mahmudi, M. Sadeghi, Correlation between shear punch and tensile strength for low-carbon steel and stainless steel sheets, J. Mater. Eng. Perform. 22 (2013) 433–438. doi:10.1007/s11665-012-0256-6.

[53] G. Mani, M.D. Feldman, D. Patel, C.M. Agrawal, Coronary stents: A materials perspective, Biomaterials. 28 (2007) 1689–1710. doi:10.1016/j.biomaterials.2006.11.042.

[54] Z. Xu, M. Hodgson, P. Cao, Effect of immersion in simulated body fluid on the mechanical properties and biocompatibility of sintered Fe–Mn-based alloys, Metals (Basel). 6 (2016) 309. doi:10.3390/met6120309.

[55] H. Hermawan, H. Alamdari, D. Mantovani, D. Dube, Iron – manganese : new class of metallic degradable biomaterials prepared by powder metallurgy, Powder Metall. 51 (2008) 38–45. doi:10.1179/174329008X284868.

Tables caption:

Table 1. Chemical composition of Fe-30Mn-1Ag after mechanical alloying

Table 2. Phase, crystallite size, and micro-hardness of the consolidated samples

Table 3. Corrosion parameters derived from PDP and EIS results

Table 4. Chemical composition of points indicated in Fig. 6 and Fig. 7 as measured by the EDS

Table 5. Mechanical properties of NS1A, BM1A, and MS1A

Figures caption:

Fig. 1. SEM images showing the morphology of: (a) mixture of Fe-Mn-Ag powders before milling, (b) pure iron powders after 10 h milling, (c) mixture of Fe/Mn/Ag powders after 10 h milling.

Fig. 2. SEM images showing the microstructure of: (a) NSFe, (b) NS0A, (c) NS1A, (d) NS3A, (e) MS1A, (f) BM1A after the SPS consolidation; and EDS elemental maps of BM1A for: (g) iron, (h) manganese and (i) silver.

Fig. 3. Particle size distribution of consolidated samples: (a) NSFe, (b) NS0A, (c) NS1A, (d) NS3A, (e) MS1A and (f) BM1A.

Fig. 4. XRD patterns of different consolidated samples (a, b), TEM bright-field images and SAD pattern of (c) 10 h milled powders and (d) consolidated NS1A samples, and crystallite size distribution of (e) 10 h milled powders and (f) consolidated NS1A samples.

Fig. 5. Electrochemical test results of all samples: (a) open circuit potential, (b) potentiodynamic polarization, (c) Nyquist plots, (d) potentiodynamic polarization after prolonged OCP for BM1A sample.

Fig. 6. SEM micrographs of the alloys' surface after subjected to polarization test: (a) NSFe, (b) NS0A, (c) NS1A, (d) NS3A, (e) MS1A, and (f) BM1A.

Fig. 7. SEM micrographs of the alloy's surface after subjected open circuit potential test at different period: (a) MS1A for 1 h, (b) BM1A for 1 h, (c) BM1A for 4 h, and (d) NS1A for 1 h (point analysis are in Table 4).

Fig. 8. (a) Static degradation rate of NS1A, BM1A, and MS1A, and (b) shear stress vs. normalized punch displacement of NS1A, BM1A, and MS1A samples.

Highlights:

- Bimodal Fe-Mn-Ag alloy was produced by mechanical alloying and spark plasma sintering
- It shows high strength (722 MPa) and ductility (38%) comparable to stainless steel
- The alloy improved significantly corrosion rate of Fe-based alloys to 0.88 mm/yr
- Bimodal-structure is a novel method to design Fe-based biodegradable alloys